ORNL/NRC/LTR-99/19

Contract Program or Project Title:	Heavy-Section Steel Technology (HSST) Program Engineering Technology Division
Subject of this Document	Evaluation of an Effective Elastic Modulus for *J*-to-K_J Conversion in 3-Dimensional Linear-Elastic Finite-Element Analyses
Type of Document:	Letter Report
Authors:	
	P. T. Williams B. R. Bass
Date of Document:	August 1999
Responsible NRC Individual and NRC Office or Division	S. N. M. Malik (301) 415-6007 Division of Engineering Technology, U. S. Nuclear Regulatory Commission

Prepared for the
U.S. Nuclear Regulatory Commission
Washington, D.C. 20555-0001
Under Interagency Agreement DOE 1886-N011-9B
NRC JCN B0119

OAK RIDGE NATIONAL LABORATORY
Oak Ridge, Tennessee 37831-8056
managed by
LOCKHEED MARTIN ENERGY RESEARCH CORP.
for the
U. S. DEPARTMENT OF ENERGY
under Contract No. DE-AC05-96OR22464

ORNL/NRC/LTR-99/19

Evaluation of an Effective Elastic Modulus for *J*-to-K_J Conversion in 3-Dimensional Linear-Elastic Finite-Element Analyses

P. T. Williams and B. R. Bass

Oak Ridge National Laboratory

Oak Ridge, Tennessee

Manuscript Completed – August 1999
Date Published – August 1999

Prepared for the
U.S. Nuclear Regulatory Commission
Washington, D.C. 20555-0001
Under Interagency Agreement DOE 1886-N011-9B
NRC JCN B0119

OAK RIDGE NATIONAL LABORATORY
Oak Ridge, Tennessee 37831-8056
managed by
LOCKHEED MARTIN ENERGY RESEARCH CORP.
for the
U. S. DEPARTMENT OF ENERGY
under Contract No. DE-AC05-96OR22464

Evaluation of an Effective Elastic Modulus for J-to-K_J Conversion in 3-Dimensional Linear-Elastic Finite-Element Analyses

P. T. Williams and B. R. Bass
Oak Ridge National Laboratory
Oak Ridge, Tennessee

Abstract: An evaluation study has been carried out of a procedure for calculating an effective elastic modulus governing the conversion of the energy release rate (G) per unit crack extension to a Mode I stress-intensity factor (K_I) for 3-dimensional linear-elastic finite-element analyses. The conventional methodology for converting G (or J) to K_I employs different equations depending on the assumption of either plane-strain or plane-stress conditions for the stress state at the crack tip. The intent of the procedure under study is to provide a qualitative measure of the departure of a 3-dimensional crack tip from these two possibly bounding stress/strain states.

Linear-elastic fracture mechanics calculations were carried out for six surface-flaw geometries with flaw ½-width to depth aspect ratios ranging from $0.75 \leq c/a \leq 3.0$ and relative flaw depths of $0.2 \leq a/t \leq 0.5$. The converted K_J profiles were benchmarked against K_I solutions published in the 1980s with close agreement relative to the shape of the curves and with $\pm 5\%$ agreement relative to magnitude. The interpolated K_J^* results generally indicated a qualitative departure from the commonly applied plane-strain conversion with an approximately uniform shift down towards the plane-stress curve.

1. Introduction

A procedure has been proposed for calculating an effective elastic modulus governing the conversion of the energy release rate (G) per unit crack extension to a Mode I stress-intensity factor (K_I) for 3-dimensional linear-elastic finite-element analyses. The conventional methodology for converting G (or J) to K_I employs different equations depending on the assumption of either plane-strain or plane-stress conditions for the stress state at the crack tip. For a 2-dimensional analysis, these plane strain or plane stress conditions are set explicitly when the model is created by the selection of appropriate finite elements. For a 3-dimensional analysis, however, these stress/strain states exist only as idealized conditions which the model may (or may not) approximately approach depending upon the significance of any 3-dimensional effects. In the proposed procedure, an effective elastic modulus for the conversion will be estimated from a computation involving opening-mode displacements of the crack face near the tip of the crack. The intent of this procedure is to provide a qualitative measure of the departure of a 3-dimensional crack tip from these two possibly bounding stress/strain states.

In the following sections, the procedure will be derived from linear-elastic stress/strain relations and fundamental concepts in linear elastic fracture mechanics (LEFM). The procedure is then evaluated through applications to 3-dimensional finite-element models.

2. Conversion of J to K_I

2.1 Conventional Methodology

The current methodology for applying finite-element modeling of both linear-elastic fracture mechanics (LEFM) and elastic-plastic fracture mechanics (EPFM) problems typically involves the calculation of the J-integral as a characterization of the *crack driving force*. Finite-element stress analysis codes such as ABAQUS [1] and WARP3D [2] calculate this fracture mechanics parameter by the Domain Integral Method [3,4] which for the most part has replaced the earlier Virtual Crack Extension technique [5,6]. For linear-elastic analyses, LEFM Mode I stress intensity factors, K_I, can readily be determined from the energy release rate interpretation of the J-integral given specific assumptions regarding the stress state near the crack tip.

Irwin [7]showed in 1957 that the Mode I stress intensity factor K_I is related to the elastic strain energy release rate, G, by

$$K_I^{\ 2} = E^* G \tag{1}$$

where the elastic modulus, E^*, for *plane stress* is

$$E^* = E \tag{2}$$

and for *plane strain* is

$$E^* = \frac{E}{\left(1-\nu^2\right)} \tag{3}$$

In Eqs. (2) and (3), E is Young's modulus and ν is Poisson's ratio. Under the conditions of LEFM, it has been shown [8] that the J-integral is equivalent to the elastic strain energy release rate, i.e., $J = G$, and from Eq. (1), therefore,

$$K_I = +\sqrt{E^* J} \tag{4}$$

As discussed in [2], for 2-dimensional analyses, the J-integral sets the amplitude of the singular stress field near the tip of a sharp Griffith crack (described by the well-known HRR solutions) under certain limiting conditions involving material constitutive behavior and the extent of plastic deformation relative to the uncracked ligament size. The choice of either Eq. (2) or Eq. (3) for the effective elastic modulus is governed by the explicit stress-state condition applied in the development of the 2-dimensional model. In 3-dimensions however, the choice of an appropriate conversion relation is somewhat problematic. The character of 3-dimensional near-tip stress/strain fields remains a subject of fracture mechanics research. Far from free-surfaces, the crack tip stress/strain fields may approximate those of plane strain; however, near traction-free surfaces these fields can exhibit strong 3-dimensional effects, possibly approaching a plane-stress state. Independent of the exact singular form of the near-tip fields, however, the J-integral

continues to provide an accurate estimate of the local energy release rate under LEFM conditions.

It is a common practice in 3-dimensional analyses to use Eqs. (3) and (4) (i.e., plane-strain conditions) to convert *J*-integral results into linear-elastic Mode I stress intensity factors, i.e.,

$$K_J = +\sqrt{\frac{E\,J}{\left(1-\nu^2\right)}} \tag{5}$$

This plane-strain conversion produces a K_J converted from J that is higher in magnitude than one produced by the plane-stress assumption for the same Young's modulus. For example, for a Poisson's ratio of 0.3, the plane-strain K_J is approximately 4.8% higher than the corresponding plane-stress K_J. Strictly speaking, this conversion is only valid for linear-elastic analyses; however, the same conversion is typically applied in elastic-plastic analyses including nonlinear finite-strain elastic-plastic conditions with significant constraint loss. For the latter condition, the resulting K_J should be viewed only as an alternate form of the primary fracture parameter, the *J*-integral, and not as a true stress-intensity factor.

2.2 Proposed Interpolation Procedure

The derivation of the procedure begins with the linear-elastic response of a sharp crack under a Mode I tensile load, where the crack is embedded in an infinite medium. The resulting asymptotic elastic stress and displacement fields can be expressed as functions of the applied K_I and the cylindrical coordinates (r, θ) of a reference frame with its origin at the crack tip (see Fig. 1). As derived in [9], the 2-dimensional stress and displacement fields are

$$\begin{Bmatrix} \sigma_{xx} \\ \tau_{xy} \\ \sigma_{yy} \end{Bmatrix} = \frac{K_I}{\sqrt{2\pi r}}\cos(\theta/2)\begin{Bmatrix} 1-\sin(\theta/2)\sin(3\theta/2) \\ \sin(\theta/2)\cos(3\theta/2) \\ 1+\sin(\theta/2)\sin(3\theta/2) \end{Bmatrix} \tag{6}$$

$$\begin{Bmatrix} \mathrm{u} \\ \mathrm{v} \end{Bmatrix} = \frac{K_I(1+\nu)}{E}\sqrt{\frac{r}{2\pi}}\begin{Bmatrix} \cos(\theta/2)\left[\kappa - 1 + 2\sin^2(\theta/2)\right] \\ \sin(\theta/2)\left[\kappa + 1 + 2\cos^2(\theta/2)\right] \end{Bmatrix} \tag{7}$$

where for the state of plane strain at the crack tip, $\kappa = 3 - 4\nu$, and for plane stress, $\kappa = (3 - \nu)/(1+\nu)$. Solving for the stresses and displacements in Eqs. (6) and (7) at $\theta = \pi$ results in

$$\begin{Bmatrix} \sigma_{xx} \\ \tau_{xy} \\ \sigma_{yy} \end{Bmatrix} = \begin{Bmatrix} 0 \\ 0 \\ 0 \end{Bmatrix} \tag{8}$$

$$\begin{Bmatrix} \mathrm{u} \\ \mathrm{v} \end{Bmatrix} = \begin{Bmatrix} 0 \\ \dfrac{K_I(1+\nu)(\kappa+1)}{E}\sqrt{\dfrac{r}{2\pi}} \end{Bmatrix} = \begin{Bmatrix} 0 \\ \dfrac{4K_I}{E^*}\sqrt{\dfrac{r}{2\pi}} \end{Bmatrix} \tag{9}$$

where the effective elastic modulus, E^*, is defined by Eqs. (2) and (3) given the crack-tip stress/strain states of plane stress and plane strain, respectively. Note that this position of (r, $\theta = \pi$) on the crack face (denoted as n^* in Fig. 1) is a traction-free surface with displacements only in the opening-mode direction for a 2-dimensional problem. Applying Eq. (4) produces the following relationship between E^*, J, and the displacement, v, at the position (r, $\theta = \pi$),

$$\begin{aligned} \mathrm{v}^2 &= \frac{16K_I^{\,2}}{E^{*2}}\frac{r}{2\pi} = \frac{8\,J\,r}{\pi\,E^*} \\ \therefore E^* &= \frac{8\,J\,r}{\pi\,\mathrm{v}^2} \end{aligned} \tag{10}$$

Dividing Eq. (10) by the plane strain definition of E^*, Eq. (3), and taking the positive square root results in an interpolation factor, F, that can be applied to the conventional plane-strain-converted K_J (see Eq. 5),

$$K_J^{\,*} = F\,K_J \tag{11}$$

where

$$F = \left[\frac{E^*}{E/\left(1-\nu^2\right)} \right]^{\frac{1}{2}} = \left[\frac{8\,J\,r\left(1-\nu^2\right)}{\pi\,E\,\mathrm{v}^2} \right]^{\frac{1}{2}} \tag{12}$$

The factor F may be interpreted as an interpolation factor that produces an approximate K_J* consistent both with the energetics principle of Eq. (1) and the theoretical 2-dimensional linear-elastic displacement fields of Eq. (7) at one point on the crack face, n*. This interpolation factor may be thought of as a qualitative measure of the departure of the calculated crack-tip displacement fields from an idealized plane-strain condition.

In summary, the interpolation procedure involves the following six steps for a given position on the flaw front, designated node n in Fig. (1), and a given state of loading (bending or tension):

1. calculate the linear-elastic strain energy release rate G (for $G = J$)
2. calculate K_J using the plane-strain assumption of Eq. (5)
3. calculate the distance r between the crack-tip node n and its associated monitor node n* (see Fig. 1)
4. calculate the opening-mode displacement "**v**" at n*
5. calculate the interpolation factor F by Eq. (12)
6. calculate the corrected K_J* by Eq. (11)

A modified procedure (to be discussed in the following section) involves calculating interpolation factors at several n* points and then determining a limiting F as $r \to 0$ by extrapolation of a regression equation to $r = 0$.

3. Results and Discussion

3.1 Finite-element Models

Finite-element meshes were generated for one semi-circular and four semi-elliptical surface flaws in a finite plate using the ORMGEN [10] mesh generator code. For the geometry shown in Fig. 2, two levels of mesh refinement were generated for testing the semi-circular surface flaw.

Mesh 1: 6162 nodes, 1240 isoparametric 20-node elements, 21-node crack front fan (see Fig. 2)

Mesh 2: 9277 nodes, 1920 isoparametric 20-node elements, 29-node crack front fan (see Fig. 3)

Figure 3 also gives the definitions of several mesh parameters, specifically the flaw depth, a, the flaw ½-width, c, the plate width, t, and the plate ½-thickness, b. These models were based on a focussed-fan flaw front where both *midpoint* and *quarterpoint* positions of the midside nodes were tested to simulate $1/r$ and $1/\sqrt{r}$ singularities in the calculated stress fields. The following surface-flaw geometries were investigated:

(1) $c/a = 0.75$ and $a/t = 0.5$ (see Fig. 4)
(2) $c/a = 1.0$ and $a/t = 0.5$ (see Fig. 5)
(3) $c/a = 1.25$ and $a/t = 0.5$ (see Fig. 6)
(4) $c/a = 1.5$ and $a/t = 0.5$ (see Fig. 7)
(5) $c/a = 1.5$ and $a/t = 0.2$ (see Fig. 8)

Additionally, a finite-root-tip radius (blunt-tip) model of a surface crack specimen, SC(T), under tension loading was obtained from the WARP3D [2] collection of fracture models. This model (see Fig. 9) included a standard-sized (6:1) ¼ t ($c/a = 3.0$, $a/t = 0.25$, $a = 6.35$ mm) semi-elliptical surface flaw with a finite-root-tip radius of 2.54×10^{-3} mm. The mesh consisted of 22,814 linear 8-node hexahedral elements with 25,642 nodes.

Implementation of the procedure requires the selection of displacement monitor nodes, n^*, that correspond to each of the flaw-front nodes, n. Calculations, described in Sec. 3.4, were carried out to determine the sensitivity of the resulting interpolation factors to the distance of the selected monitor node from its corresponding flaw-front node.

The following linear elastic properties were used for all of the results reported in this study: Young's modulus, $E = 206.842$ GPa (30,000 ksi) and Poisson's ratio, $\nu = 0.3$.

3.2 *J*-integral Calculations

Crack driving-force *J*-integrals were calculated for all of the models described in Sect. 3.1. Figure 10 presents the *J*-integrals for the semi-circular surface flaw under a tensile load calculated for Mesh 1 compared to those calculated for Mesh 2. In Fig. 10 (and all position-dependent plots in this report), the circular angle, θ, designates a position along the flaw front where $\theta = 0$ degrees is at the traction-free surface and $\theta =$ 90 degrees is located at the reflective symmetry plane (deepest point of the flaw). These results indicate that for this loading, the Mesh 1 and 2 solutions are effectively mesh independent. ABAQUS [1] *J*-integrals results are compared to WARP3D [2] in Fig. 11a for $0.75 \leq c/a \leq 1.5$ (a/t = 0.5), Fig. 11b for $0.2 \leq a/t \leq 0.5$, c/a = 1.5. In Fig. 12, ABAQUS and WARP3D *J*-integrals are compared for the (6:1) ¼ *t* semi-elliptical surface flaw. In both Figs. 11 and 12, the ABAQUS and WARP3D results agree very closely except at the two boundary planes.

3.3 Interpolation Factor Calculations

Displacement data, "**v**", at the monitor nodes, *n**, for the semi-circular model are shown in Figs. 13 and 14 as a function of distance from their corresponding flaw-front nodes, *n*. As expected from Eq. (10), the magnitude of the displacements increases with increasing distance, *r*, from the flaw front. Dividing the square of the displacements by the distance *r* (see Eq. (10)) as in Fig. 14 indicates a degree of sensitivity to the selection of the position of the monitor node. Due to this sensitivity, a modified procedure for estimating the interpolation factor was tested.

As shown in Fig. 15, several *F* factors were calculated at a number of points from the crack tip and plotted as a function of $(r/a)^{1/2}$. A second-order regression equation was then fit to the data and extrapolated to $(r/a)^{1/2} = 0$; the resulting intercept was then taken as the effective interpolation factor. This modified procedure worked well for deep flaws (c/a = 0.75); however, the effectiveness of the extrapolation broke down for flaws with wider aspect ratios, producing *F* values that projected the plane-strain K_J above or below the bounds of the plane-strain/plane-stress limits. For the models with $c/a \geq 1.0$, the

interpolation factor calculated for the closest available node to the crack-tip node was used.

ORMGEN [10] employs special crack tip elements along the crack front to model the appropriate singularity in the stress field. For linear elastic calculations, the *quarter-point* wedge element of Fig. 16(a) can be used at the crack front to allow for a $1/\sqrt{r}$ singularity in the stress and strain fields [11], where again r is the radial distance from the crack tip. Figure 16(b) illustrates the collapsed prism element appropriate for both linear-elastic and perfectly plastic materials, with interior nodes located at the true *midpoint* position, simulating a $1/r$ singularity at the crack front. In the collapsed (or focussed) element, the nodes that initially share the same positions at the tip will separate with increasing load to allow for blunting of the crack (see Fig. 17). Interpolation factors based on the *midpoint* and *quarter-point* options are compared in Fig. 18 for the semi-circular surface flaw using Mesh 1 with essentially identical results except for a small difference at the traction-free surface (at a circular angle of $\theta = 0$ degrees). Quarter-point results are also shown in Fig. 19 for Meshes 1 and 2, indicating a continued mesh independence (see Fig. 10).

Using the Mesh 2 refinement level with the *midpoint* option, interpolation factors at $r/a = 0.15$ were calculated for four surface-flaw geometries, $0.75 \leq c/a \leq 1.5$ ($a/t = 0.5$), under tension loading as shown in Fig. 20. For this fixed flaw depth, increasing the c/a ratio (with constant a) resulted in decreasing interpolation factors. These trends were essentially independent of the applied tensile load. For the blunt-tip (6:1)-¼ t model, the interpolation factors at $r/a = 0.0004$ were approximately independent of the position along the flaw front as shown in Fig. 20.

3.4 Tangential and Perpendicular Strain Distributions

The minimum and intermediate principal strains are plotted as a function of position along the flaw front for both the sharp-tip models in Fig. 22 and the blunt-tip model in Fig. 23. The minimum principal strain corresponds effectively to the extensional strain that is tangent to the flaw front, and the intermediate principal strain corresponds to the extensional strain perpendicular to the locus of the flaw front within the flaw-front plane. For a Mode I tensile loading, the tangential strains should be consistently compressive along the length of the flaw front with an increase in the absolute value as the flaw front approaches the traction-free surface, thereby demonstrating qualitatively a loss of constraint relative to the deepest point of the flaw.

3.5 K_I and K_J* Results

In Figs. 24-30, applied stress-intensity factors, K_J, normalized by the nominal loading stress (σ_t) and the square root of the flaw depth, a, are compared to the stress-intensity factor, K_I, results of Newman and Raju [12]. In the 1980s, Newman and Raju [12] calculated stress intensities directly from their finite-element solutions of the stress-fields near the crack tip, rather than calculating a J-integral with subsequent conversion. For all of the geometries studied, the converted K_J distributions closely follow the shapes of the Newman-Raju profiles, and the offsets between K_J and K_I are typically less than the magnitude of the difference between the plane-strain/plane-stress limits (< 5%). For a fixed flaw depth of a/t = 0.5, Figs. 24-28 indicate that increasing the aspect ratio (c/a) from 0.75 to 1.5 results in an upward shift of the K_J curves relative to the position of the Newman-Raju curves.

Results for the c/a = 0.75 model are presented in Figs. 24 and 25. In Fig. 24, the interpolation factor was calculated using displacement results from a monitor node at a distance of r/a = 0.0188 from the crack-tip node. The extrapolation procedure described in Sect. 3.3 was applied for the results shown in Fig. 25, and the resulting K_J^* values indicate an approximate plane-strain condition near the deepest point in the flaw that gradually shifts to an approximate plane-stress state as the flaw front approaches the traction-free surface. For the geometries in Figs. 26-29, the interpolation factor shifts the

plane-strain converted K_J down towards the plane-stress curve for the full length of the flaw front.

The results for the finite-root-tip radius (blunt-tip) model (c/a = 3.0 and a/t = 0.25) of Fig. 9 are plotted in Fig. 30. The positions of the plane-strain/plane-stress curves relative to the Newman-Raju curve are consistent with the other shallow-flaw geometry with a sharp-tip flaw front (see Fig. 29). The interpolation factor shifted the plane-strain K_J down to (or slightly below) the plane-stress curve.

4. Summary and Conclusions

An evaluation study has been carried out of a procedure for calculating an effective elastic modulus governing the conversion of the energy release rate (G) per unit crack extension to a Mode I stress-intensity factor (K_I) for 3-dimensional linear-elastic finite-element analyses. The conventional methodology for converting G (or J) to K_I employs different equations depending on the assumption of either plane-strain or plane-stress conditions for the stress state at the crack tip. The intent of the procedure under study is to provide a qualitative measure of the predicted departure of a 3-dimensional crack tip from these two possibly bounding stress/strain states.

Linear-elastic stress analysis and fracture mechanics calculations were carried out for six surface-flaw geometries with flaw ½-width to depth aspect ratios ranging from $0.75 \leq c/a \leq 3.0$ and relative flaw depths of $0.2 \leq a/t \leq 0.5$. The converted K_J profiles were benchmarked against K_I solutions published in the 1980s with close agreement relative to the shape of the curves and with $\pm$5% agreement relative to magnitude. The interpolated K_J^* results generally indicated a qualitative departure from the commonly applied plane-strain conversion with an approximately uniform shift down towards the plane-stress curve.

Acknowledgments

The procedure evaluated in this study was originally formulated and proposed by J. G. Merkle.

References

[1] *ABAQUS Theory Manual, Version 5.8*, Hibbit, Karlson and Sorensen, Inc., Providence, RI, 1998.

[2] K. C. Koppenhoefer, A. S. Gullerud, C. Ruggieri, R. H. Dodds, Jr., and B. E. Healy, *WARP3D- Release 11.0 Dynamic Nonlinear Analysis of Solids Using a Preconditioned Conjugate Gradient Software Architecture*, UILU-ENG-95-2012, University of Illinois at Urbana-Champaign, Urbana, Illinois, November 1998.

[3] F. Z. Li, C. F. Shih, and A. Needleman, "A Comparison of Methods for Calculating Energy Release Rates," *Engineering Fracture Mechanics*, **21**, (1985) 405-421.

[4] B. Moran and C. F. Shih, "A General Treatment of Crack Tip Contour Integrals," *International Journal of Fracture* **35**, (1987) 295-310.

[5] T. K. Hellen, "On the Method of Virtual Crack Extension," *International Journal for Numerical Methods in Engineering* **9**, (1975) 187-207.

[6] D. M. Parks, "The Virtual Crack Extension Method for Nonlinear Material Behavior," *Computer Methods in Applied Mechanics and Engineering* **12**, (1977) 353-364.

[7] G. R. Irwin, "Analysis of Stresses and Strains Near the End of a Crack Traversing a Plate," *Journal of Applied Mechanics* **24**, (1957) 361-364.

[8] J. Rice, "A Path Independent Integral and the Approximate Analysis of Strain Concentration by Notches and Cracks," *Journal of Applied Mechanics* **16**, (1968) 1-12.

[9] M. F. Kanninen and C. H. Popelar, *Advanced Fracture Mechanics*, Oxford University Press, New York, 1985.

[10] B. R. Bass and J. W. Bryson, Jr., *Applications of Energy Release Rate Techniques to Part-Through Cracks in Plates and Cylinders, ORMGEN-3D: A Finite Element Mesh Generator for 3-Dimensional Crack Geometries*, NUREG/CR-2997(ORNL/TM-8527/V1), Union Carbide, Nuclear Corp., Oak Ridge National Laboratory, December 1982.

[11] R. S. Barsoum, "Triangular Quarter-Point Elements as Elastic and Perfectly-Plastic Crack Tip Elements," *Int. J. Numer. Methods Engr.* **11**, 85-98 (1977).

[12] J. C. Newman and I. S. Raju, "Stress-Intensity Factor Equations for Cracks in Three-Dimensional Finite Bodies Subjected to Tension and Bending Loads," in *Computational Methods in the Mechanics of Fracture*, ed. by S. N. Atluri, Vol. 2 in *Computational Methods in Mechanics*, North Holland (1986) 311-334.

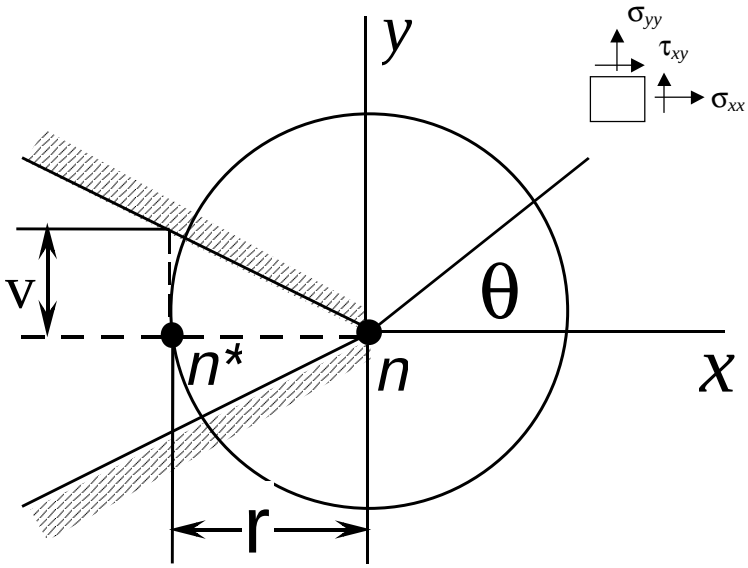

Fig. 1. Geometry of linear elastic sharp crack showing location of crack tip node, *n*, and crack-displacement monitor node, *n**.

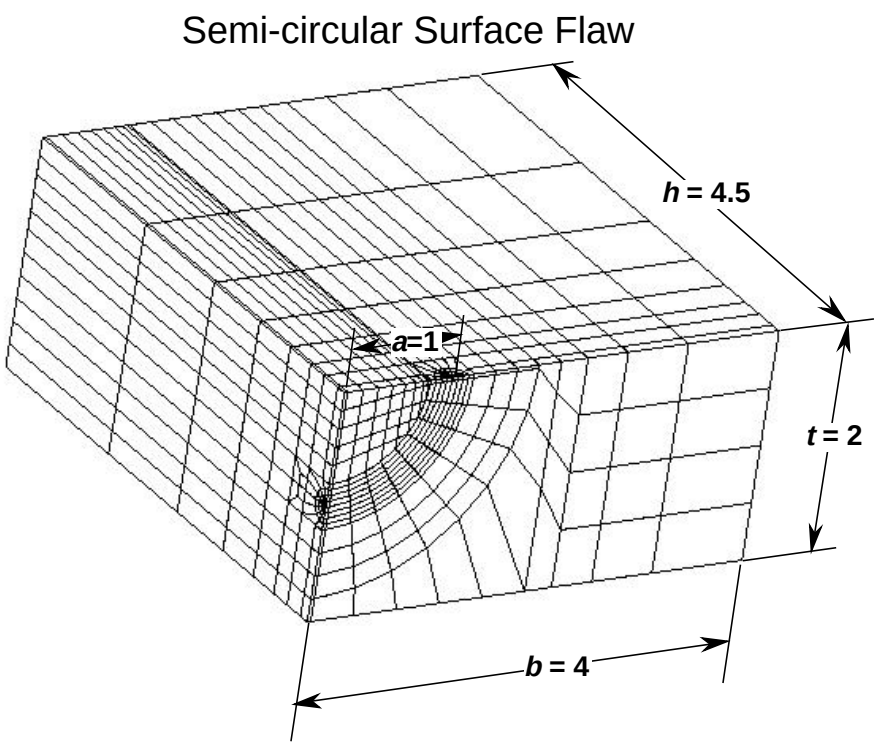

Fig. 2. Meshes for semi-circular surface flaw with *a/t* = 0.5:
Mesh 1: 1240 elements, 6162 nodes, 21 node crack front fan

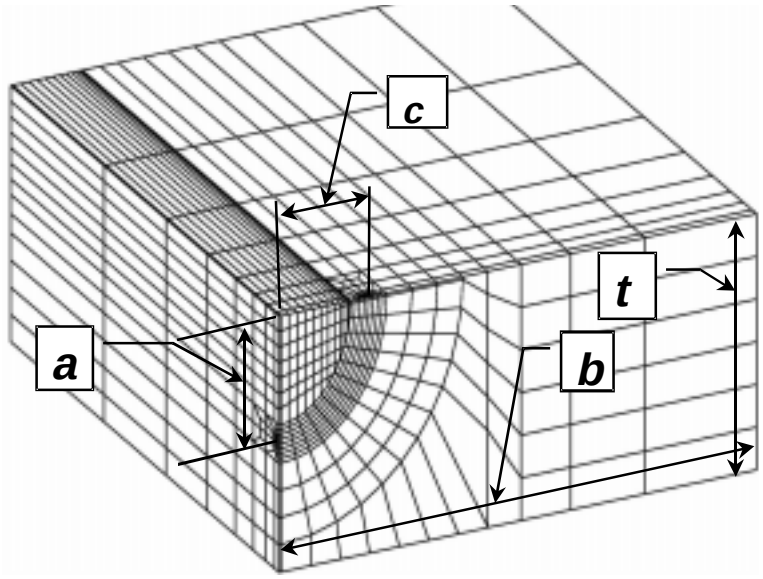

Fig. 3. Mesh parameter definitions for semi-elliptical surface flaws
Mesh 2: 1920 elements, 9277 nodes, 29 node crack front fan.

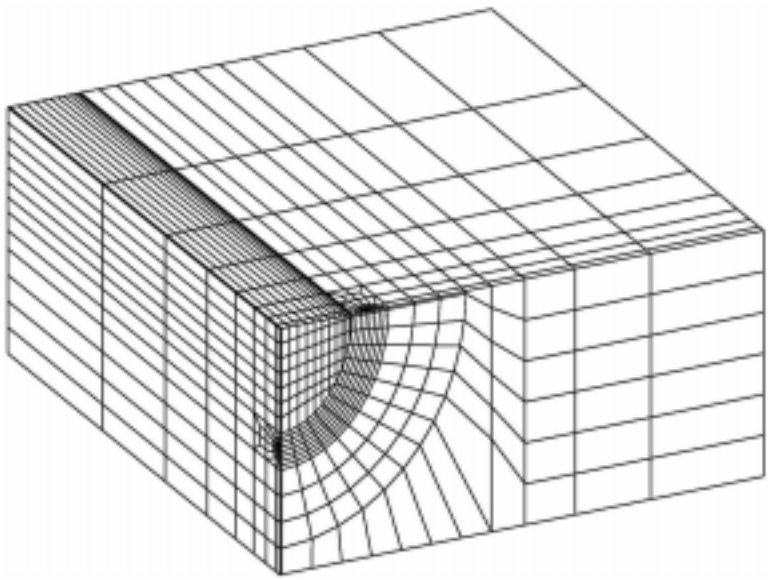

Fig. 4. Semi-elliptical surface flaw: c/a = 0.75, a/t = 0.5 (Mesh 2).

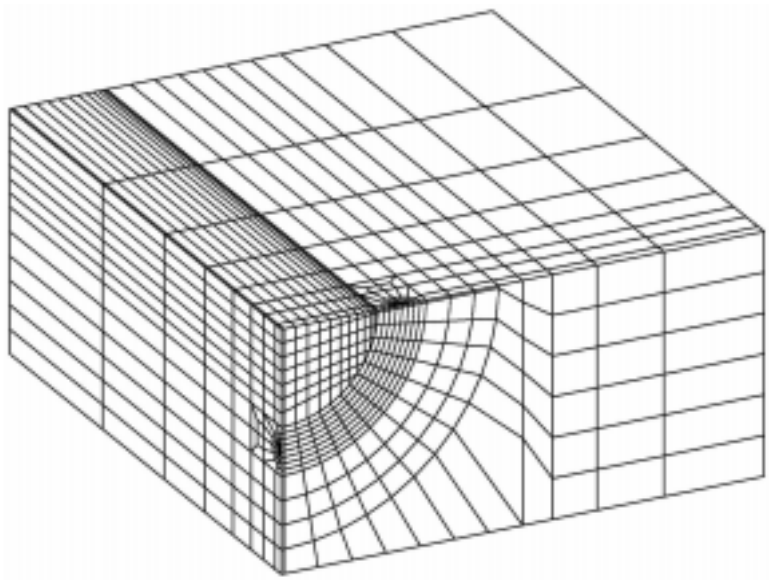

Fig. 5. Semi-circular surface flaw: *c/a* = 1.0, *a/t* = 0.5 (Mesh 2).

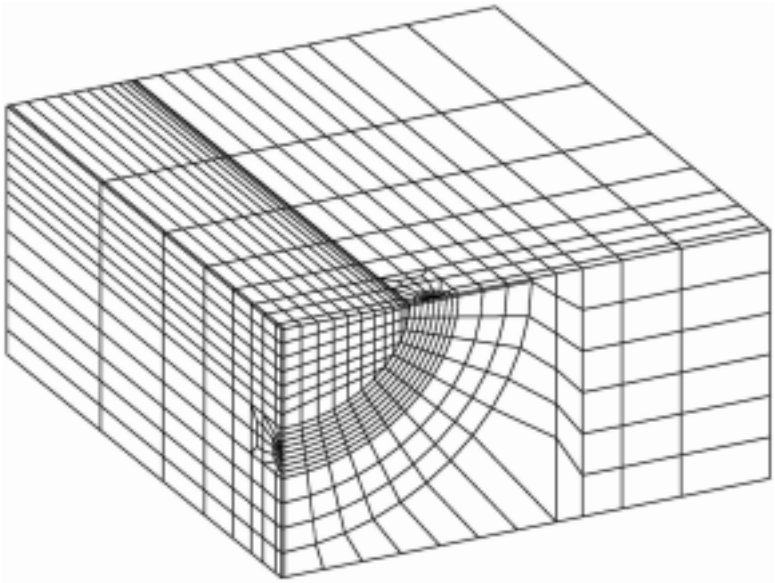

Fig. 6. Semi-elliptical surface flaw: *c/a* = 1.25, *a/t* = 0.5 (Mesh 2).

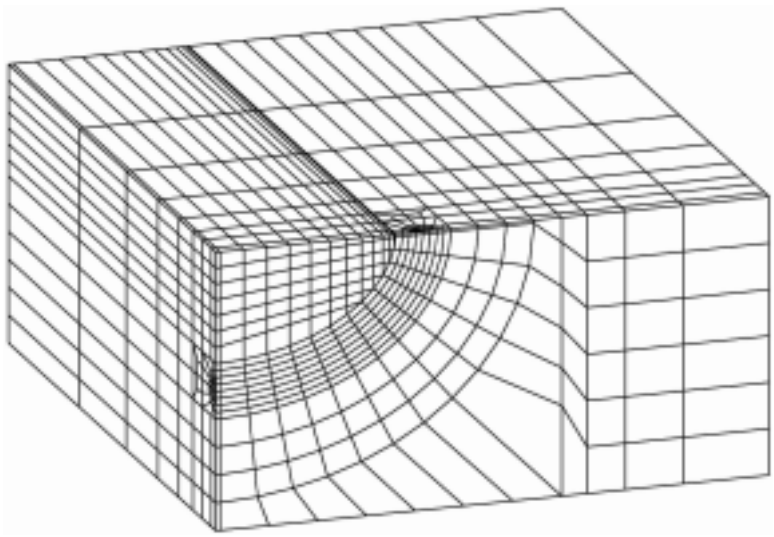

Fig. 7. Semi-elliptical surface flaw: *c/a* = 1.5, *a/t* = 0.5 (Mesh 2).

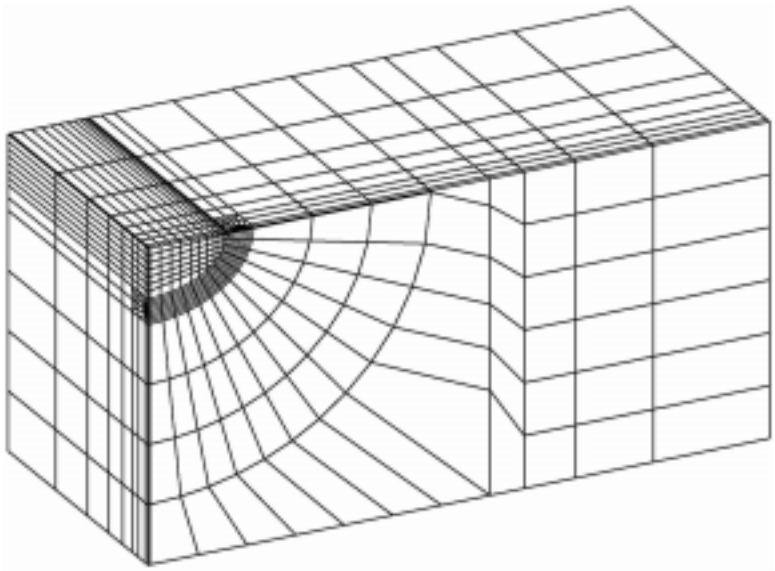

Fig. 8. Semi-elliptical surface flaw: *c/a* = 1.5, *a/t* = 0.2 (Mesh 2).

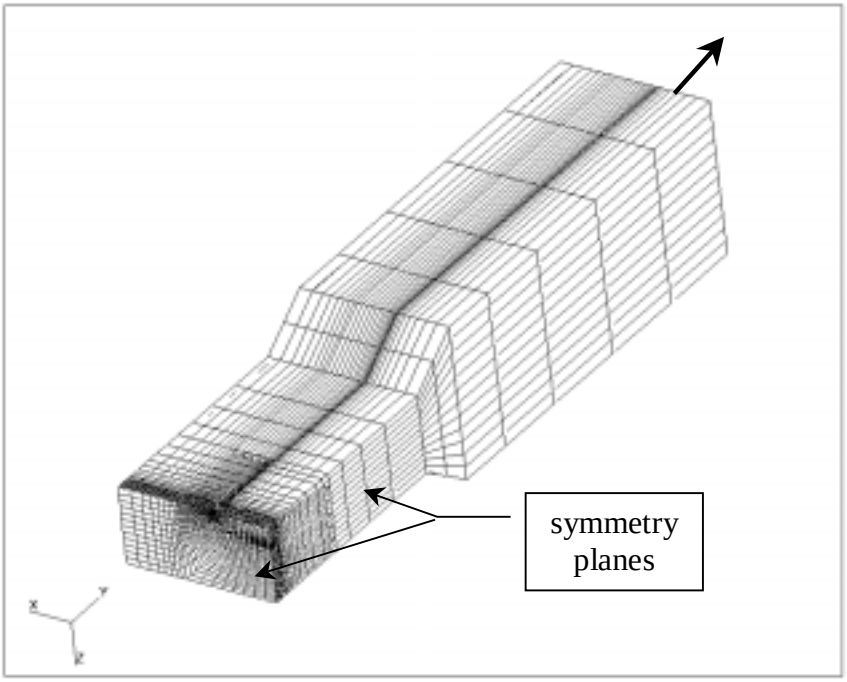

(a)

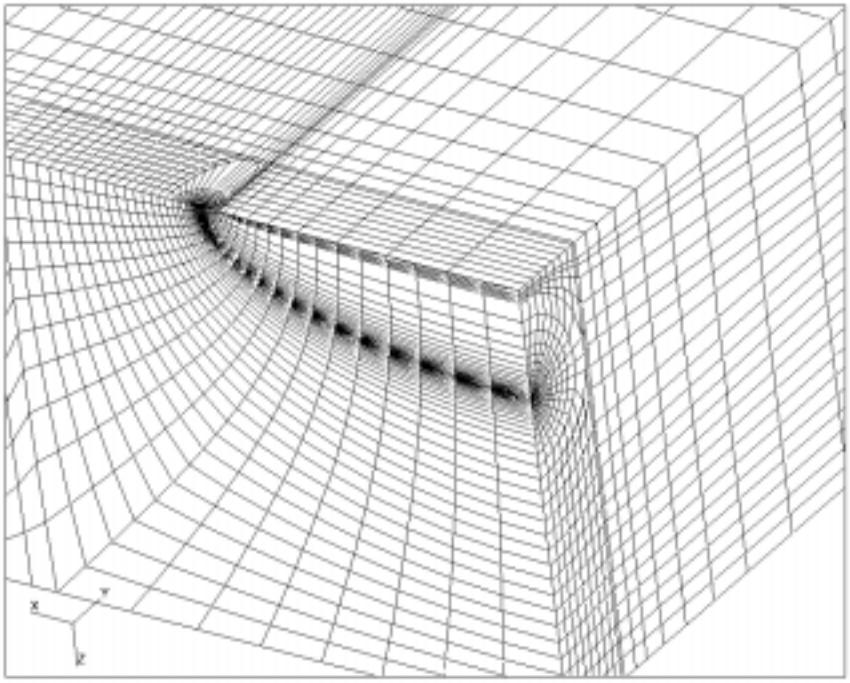

(b)

Fig. 9. Finite-root tip semi-elliptical surface flaw (2c/a =6, a/t = 0.25 under tension loading) in an SC(T) specimen: (a) complete model and (b) closeup of (6:1) ¼*t* surface flaw (25,642 nodes and 22,814 linear 8-node hexahedral elements).

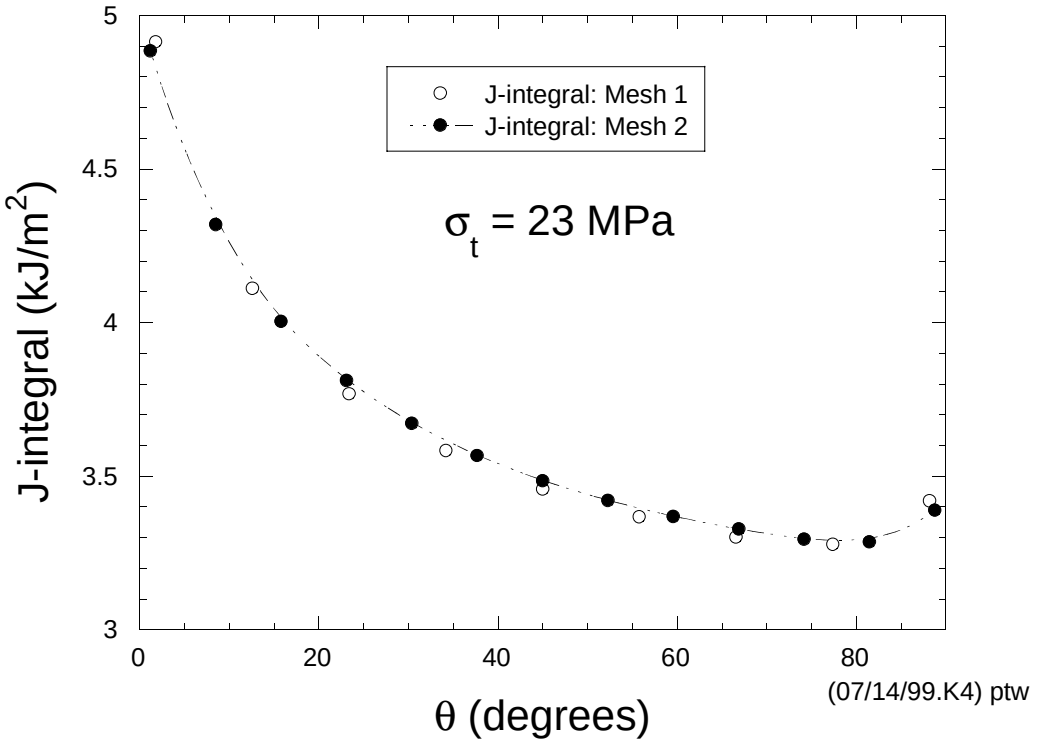

Fig. 10. Comparison of *J*-integral results for two meshes of semi-circular surface flaw.

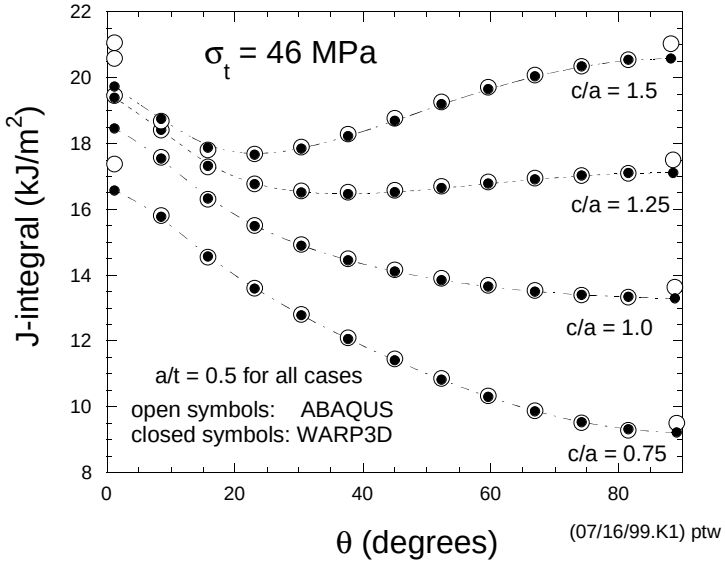

(a)

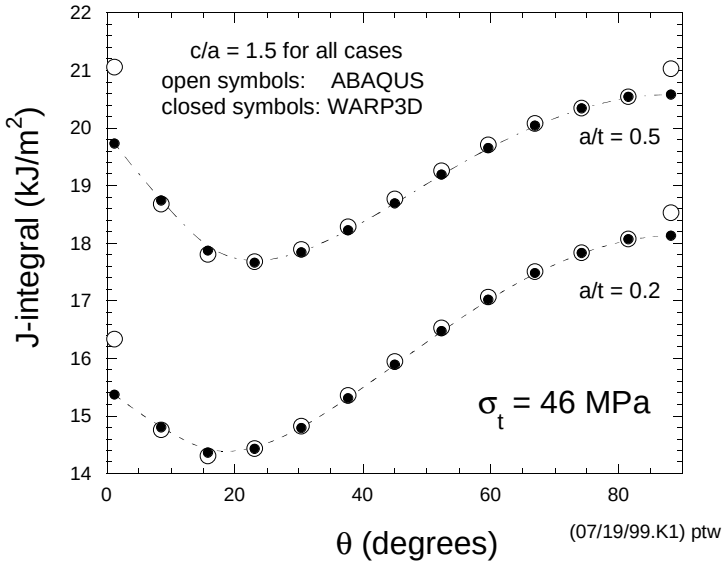

(b)

Fig. 11. Comparison of ABAQUS *J*-integral results to WARP3D results for σ = 46 MPa.: (a) $0.75 \leq c/a \leq 1.5$ (a/t = 0.5), (b) $0.2 \leq a/t \leq 0.5$, c/a = 1.5.

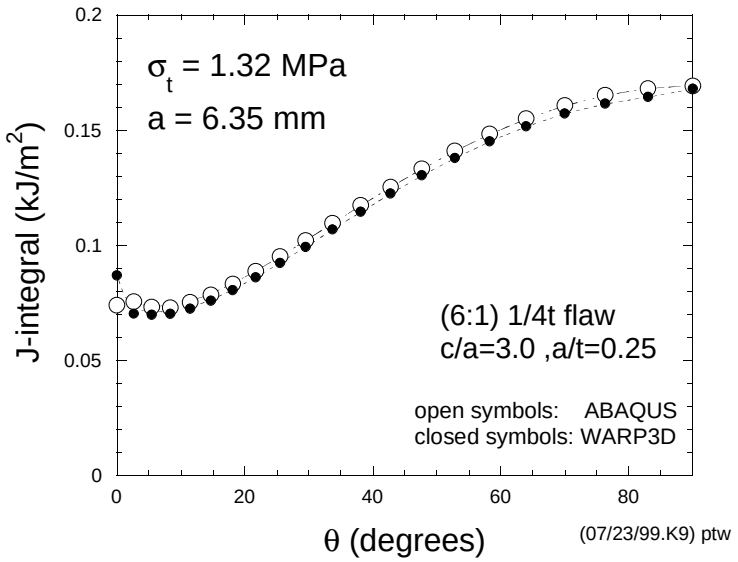

Fig. 12. Comparison of ABAQUS *J*-integral results to WARP3D results for σ = 1.32 MPa tensile load of (6:1) ¼ *t* semi-elliptical surface flaw.

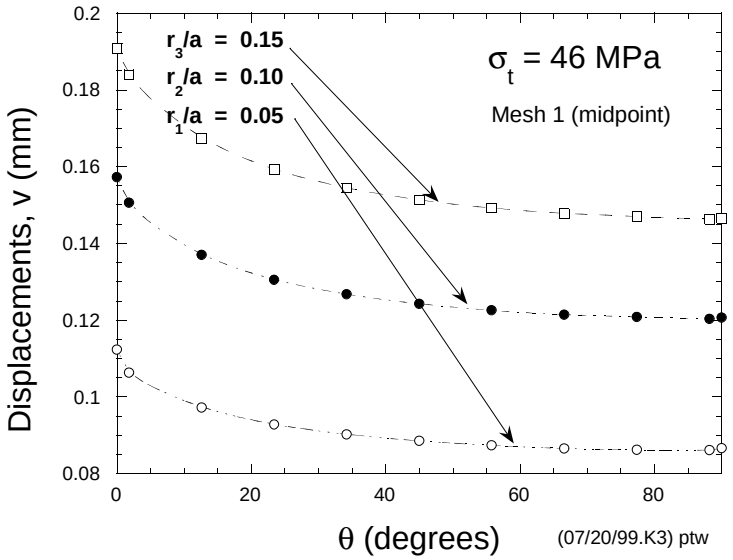

Fig. 13. Variation of displacement profiles with distance of monitor node, *n**, from crack tip node, *n*, for semi-circular surface flaw (*c/a* = 1).

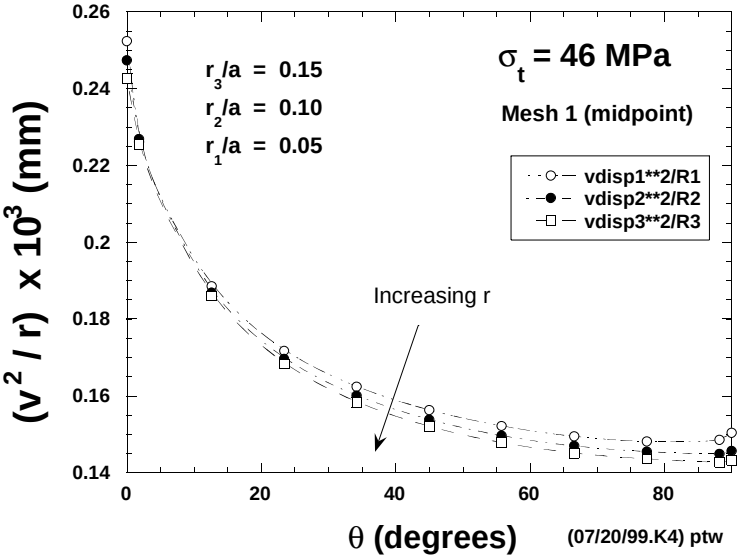

Fig. 14. Dependence of v^2/r factor with with distance of monitor node, *n**, from crack tip node, *n*, for semi-circular surface flaw (*c/a* = 1).

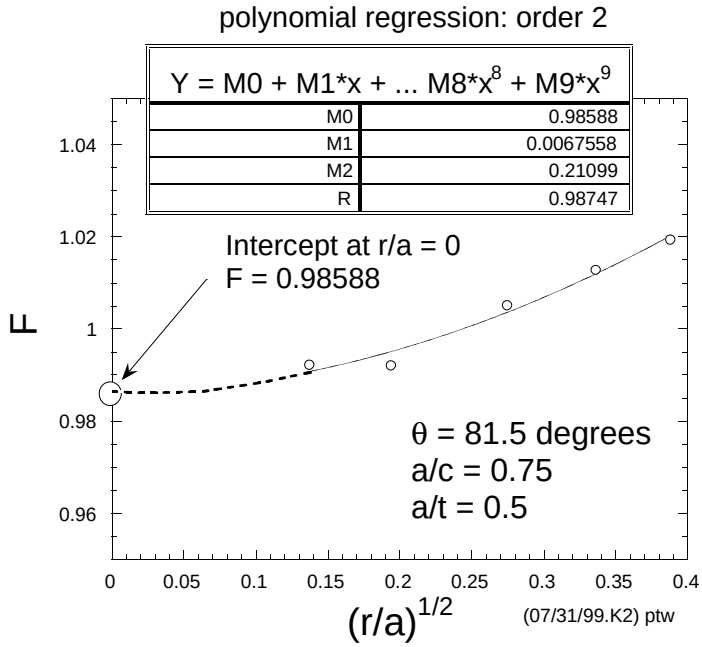

Fig. 15. Variation of interpolation factor (at θ = 81.5 degrees) with distance of monitor node, *n**, from crack tip node, *n*, for surface flaw with *c/a* = 0.75, *a/t* = 0.5.

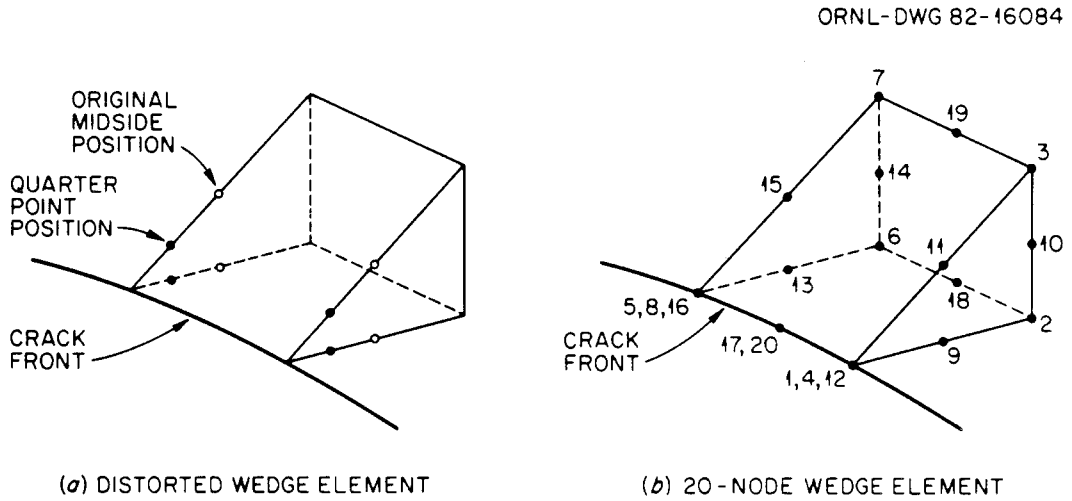

Fig. 16. Special crack tip elements employed in ORMGEN [10].

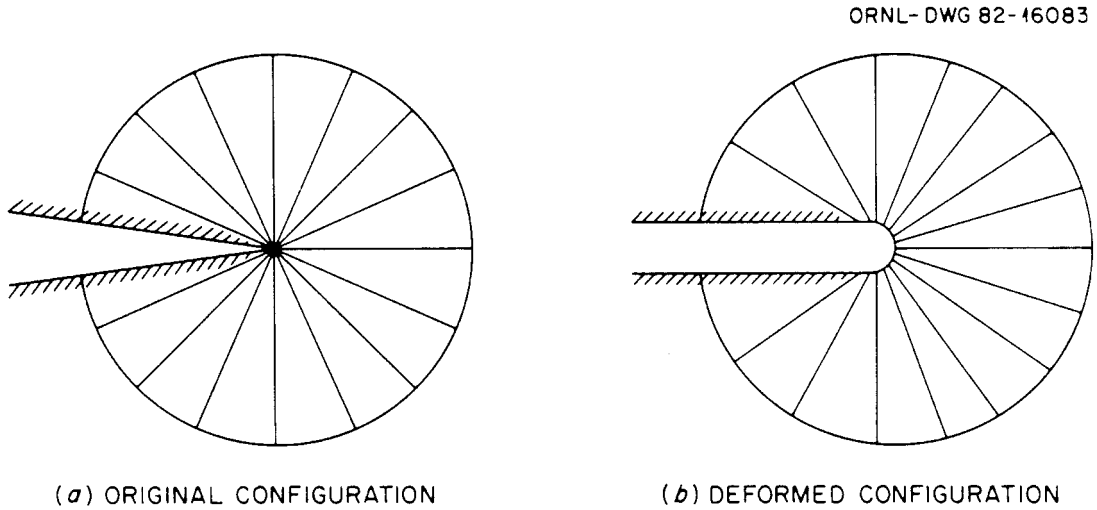

Fig. 17. Collapsed prism elements.

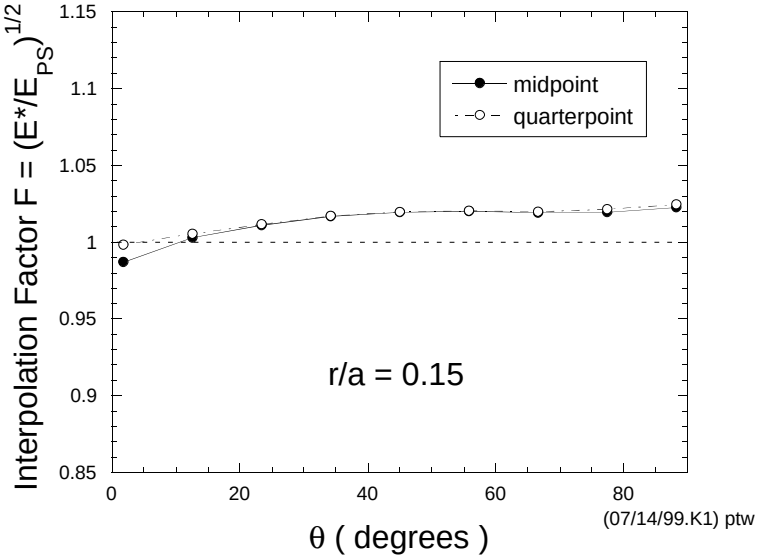

Fig. 18. Comparison of interpolation factors (at *r/a* = 0.15) for placement of midside nodes for elements in flaw-front fan: midpoint placement compared to quarterpoint placement (semi-circular surface flaw: Mesh 1).

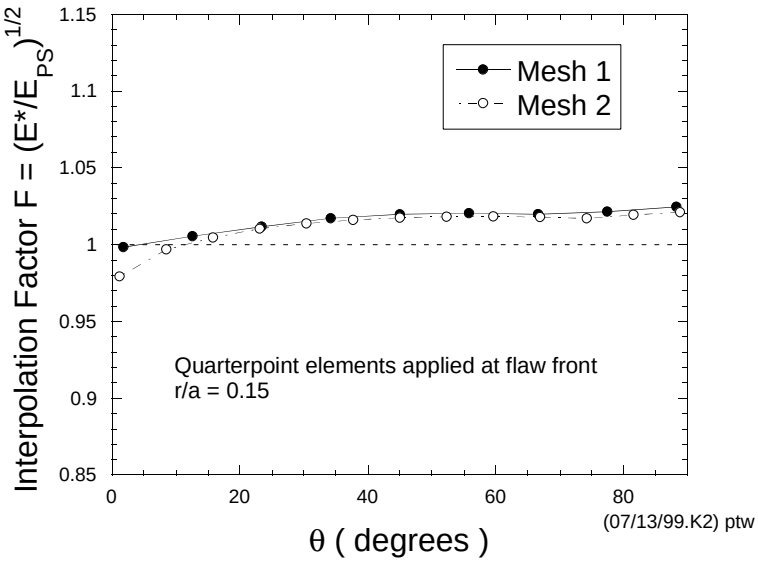

Fig. 19. Interpolation factor at *r/a* = 0.15 for semi-circular surface flaw (*a*/*t* = 0.5) under tension loading.: comparison of Mesh 1 to Mesh 2 results.

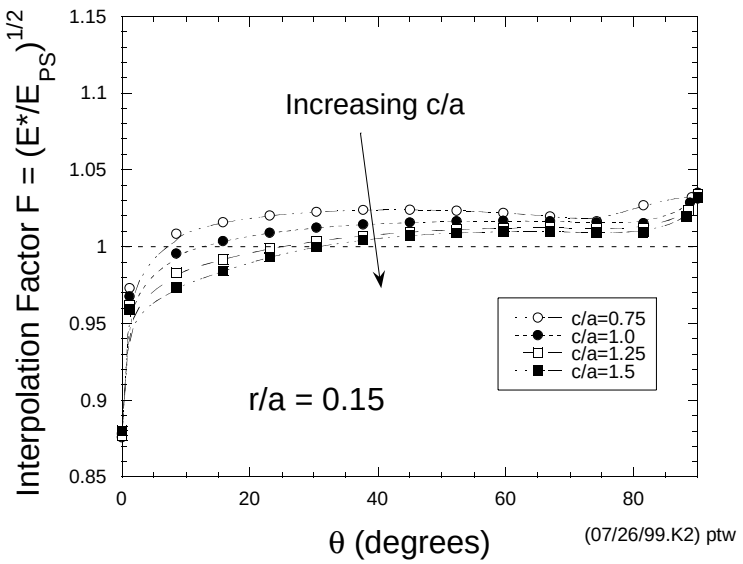

Fig. 20. Interpolation factors at *r/a* = 0.15 for *a/t* = 0.5 and increasing *c/a*.

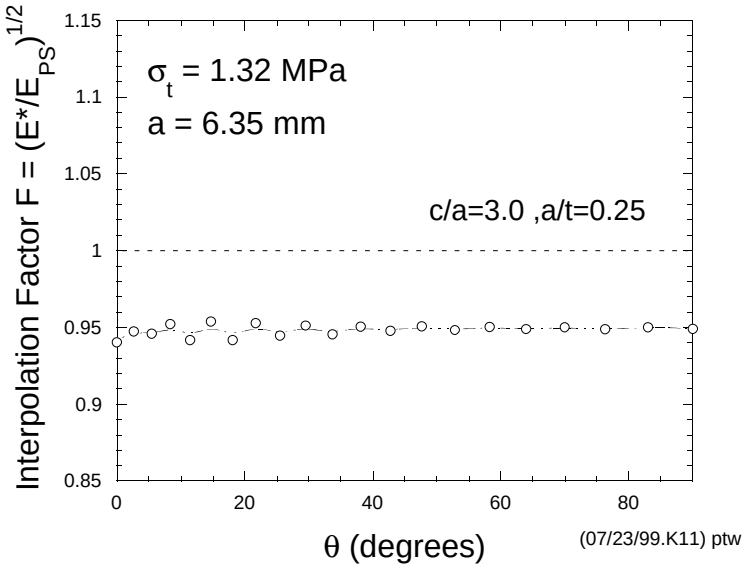

Fig. 21. Interpolation factor at *r/a* = 0.0004 for semi-elliptical (6:1)-¼ *t* surface flaw under tension loading.

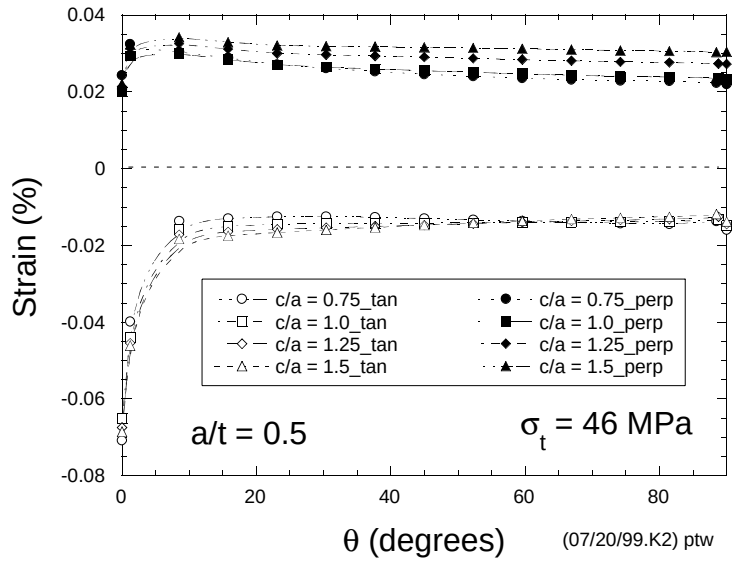

Fig. 22. Variation of tangential and perpendicular strains along crack front for semi-elliptical and semi-circular flaws with $0.75 \leq (c/a) \leq 1.5$.

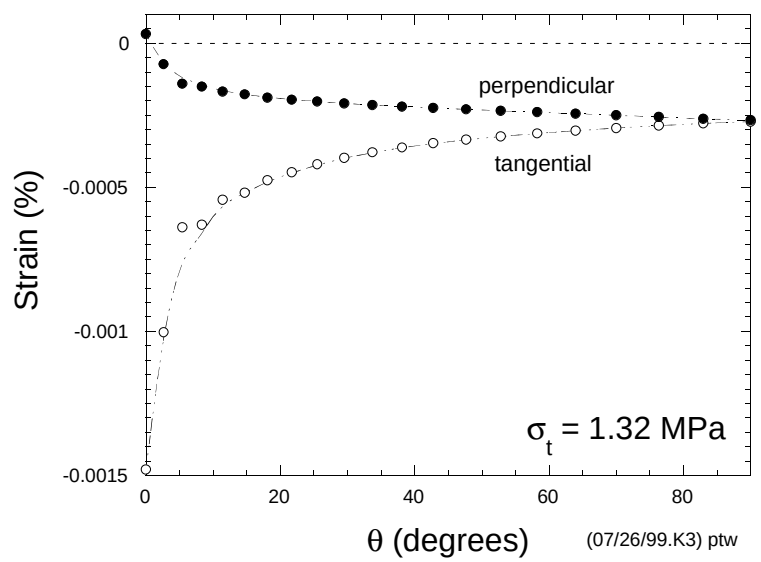

Fig. 23. Variation of tangential and perpendicular strains along crack front for semi-elliptical (6:1) - ¼ *t* surface flaw with finite-root tip flaw.

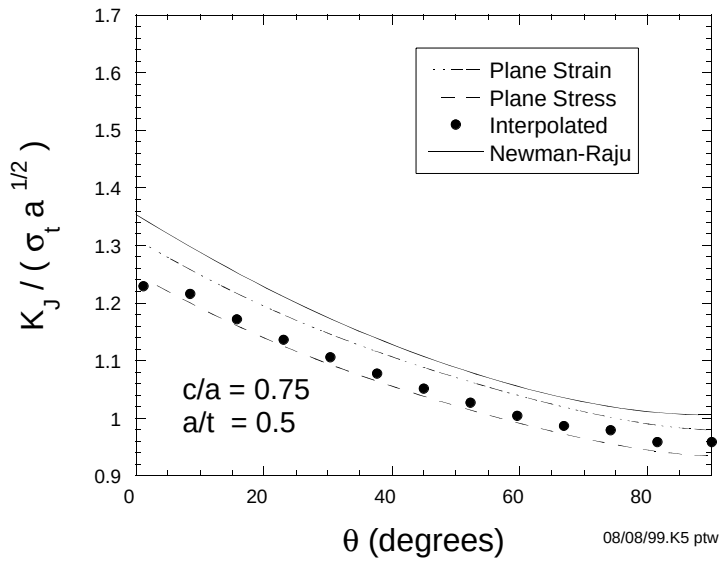

Fig. 24. Normalized Newman-Raju K_I results compared to finite-element solutions with plane strain, plane stress, and interpolated K_J values for $c/a = 0.75$ ($a/t = 0.5$) under tension loading using Mesh 2: interpolation factors taken from monitor node at $r/a = 0.0188$.

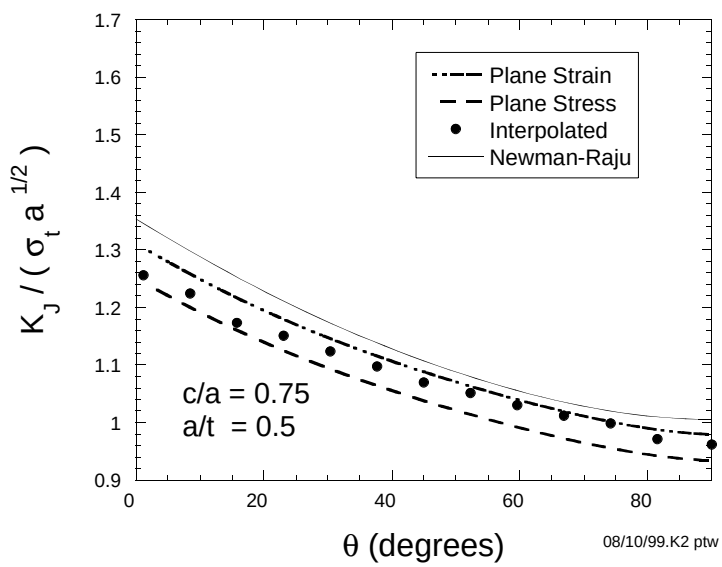

Fig. 25. Normalized Newman-Raju K_I results compared to finite-element solutions with plane strain, plane stress, and interpolated K_J values for $c/a = 0.75$ ($a/t = 0.5$) under tension loading using Mesh 2: interpolation factors extrapolated from monitor nodes at $0.0188 \leq r/a \leq 0.4$.

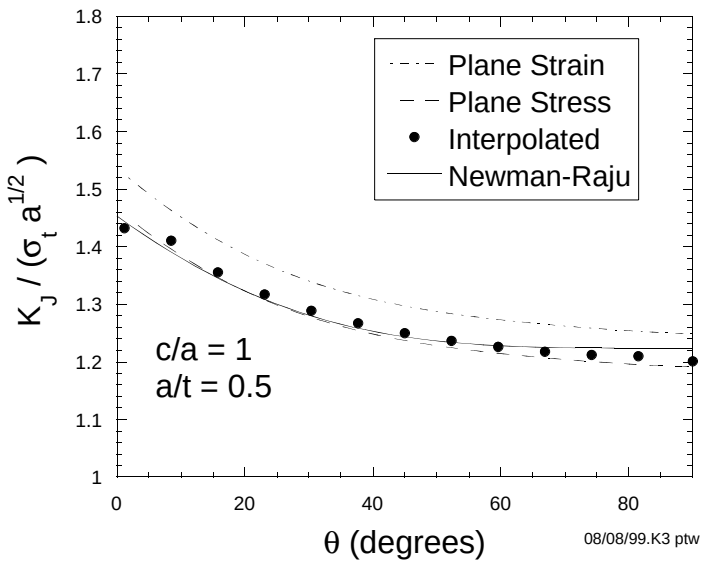

Fig. 26. Normalized Newman-Raju K_I results compared to finite-element solutions with plane strain, plane stress, and interpolated K_J values for c/a = 1.0 (a/t = 0.5) under tension loading using Mesh 2: interpolation factors taken from monitor node at r/a = 0.0188.

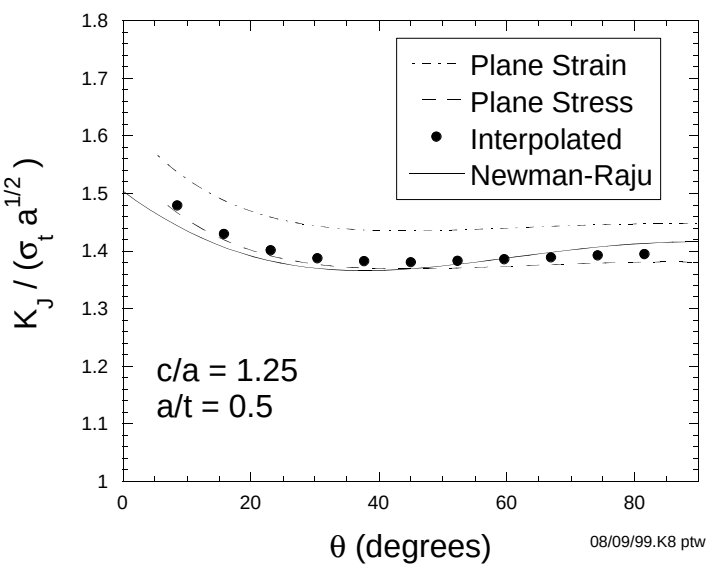

Fig. 27. Normalized Newman-Raju K_I results compared to finite-element solutions with plane strain, plane stress, and interpolated K_J values for c/a = 1.25 (a/t = 0.5) under tension loading using Mesh 2: interpolation factors taken from monitor node at r/a = 0.0188.

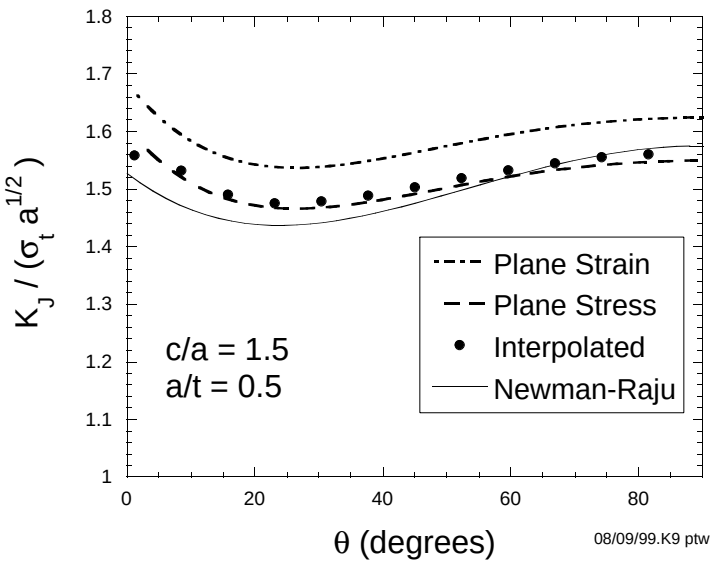

Fig. 28. Normalized Newman-Raju K_I results compared to finite-element solutions with plane strain, plane stress, and interpolated K_J values for c/a = 1.5 (a/t = 0.5) under tension loading using Mesh 2: interpolation factors taken from monitor node at r/a = 0.0188.

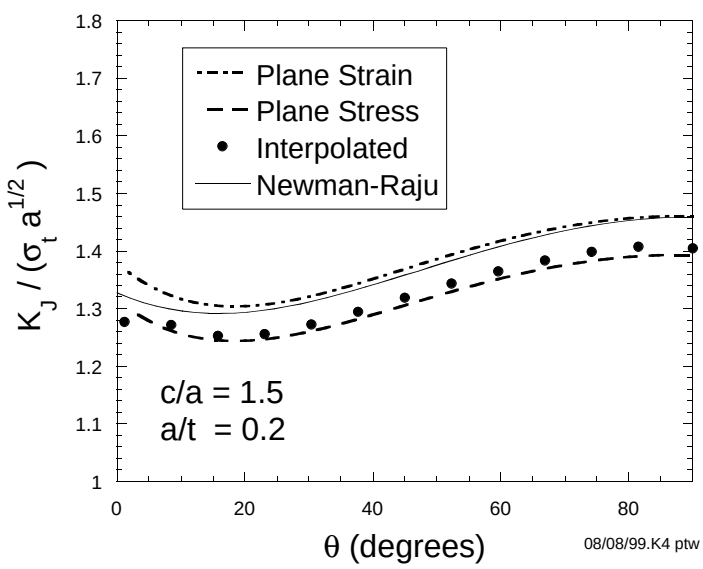

Fig. 29. Normalized Newman-Raju K_I results compared to finite-element solutions with plane strain, plane stress, and interpolated K_J values for c/a = 1.5 (a/t = 0.2) under tension loading using Mesh 2: interpolation factors taken from monitor node at r/a = 0.0188.

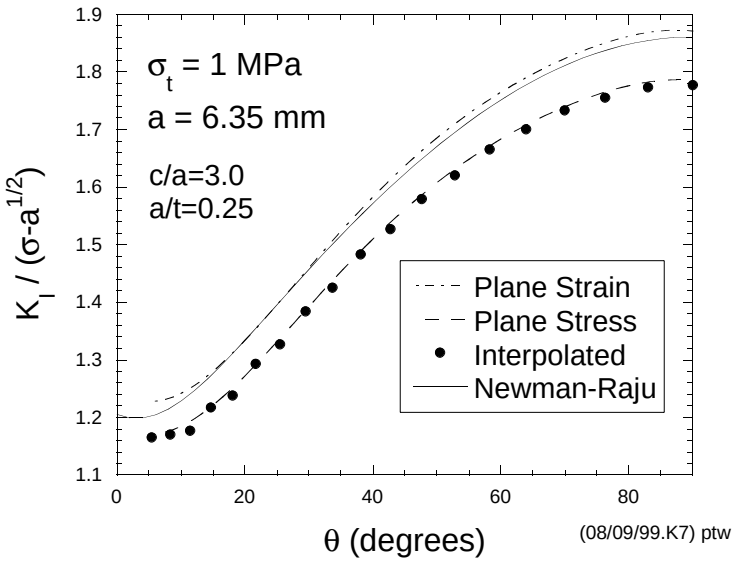

Fig. 30 Normalized Newman-Raju K_I results compared to finite-element solutions with plane strain, plane stress, and interpolated K_J values for c/a = 3.0 (a/t = 0.25) under tension loading using Mesh 2: interpolation factors taken from monitor node at r/a = 0.0004.

DISTRIBUTION

01-05. B. R. Bass
06. W. G. Craddick
07. K. W. Childs
08. T. L. Dickson
09. E. M. Hackett, NRC/DET/RES/MEB
10. D. M. Hetrick
11-13. S. N. M. Malik, NRC/DET/RES/MEB
14. M. E. Mayfield /NRC/DET/RES/MEB
15. W. J. McAfee
16. R. K. Nanstad
17. C. E. Pugh
18. C. G. Santos, NRC/DET/RES/MEB
19-23. P. T. Williams
24. Laboratory Records
25. File-RC